molecules

MDPI

Article

Optimisation of the Flame Spheroidisation Process for the Rapid Manufacture of Fe_3O_4-Based Porous and Dense Microspheres

Jesús Molinar-Díaz [1], John Luke Woodliffe [1], Elisabeth Steer [2], Nicola A. Morley [3], Paul D. Brown [1,2] and Ifty Ahmed [1,*]

[1] Advanced Materials Research Group, Faculty of Engineering, University of Nottingham, University Park, Nottingham NG7 2RD, UK
[2] Nanoscale and Microscale Research Centre, University of Nottingham, University Park, Nottingham NG7 2RD, UK
[3] Department of Materials Science and Engineering, University of Sheffield, Sheffield S1 3JD, UK
* Correspondence: ifty.ahmed@nottingham.ac.uk

Abstract: The rapid, single-stage, flame-spheroidisation process, as applied to varying Fe_3O_4:$CaCO_3$ powder combinations, provides for the rapid production of a mixture of dense and porous ferromagnetic microspheres with homogeneous composition, high levels of interconnected porosity and microsphere size control. This study describes the production of dense (35–80 μm) and highly porous (125–180 μm) $Ca_2Fe_2O_5$ ferromagnetic microspheres. Correlated backscattered electron imaging and mineral liberation analysis investigations provide insight into the microsphere formation mechanisms, as a function of Fe_3O_4/porogen mass ratios and gas flow settings. Optimised conditions for the processing of highly homogeneous $Ca_2Fe_2O_5$ porous and dense microspheres are identified. Induction heating studies of the materials produced delivered a controlled temperature increase to 43.7 °C, indicating that these flame-spheroidised $Ca_2Fe_2O_5$ ferromagnetic microspheres could be highly promising candidates for magnetic induced hyperthermia and other biomedical applications.

Keywords: magnetite; magnetic particles; porous microspheres; calcium ferrites; flame spheroidisation; ceramics; magnetic hyperthermia

Citation: Molinar-Díaz, J.; Woodliffe, J.L.; Steer, E.; Morley, N.A.; Brown, P.D.; Ahmed, I. Optimisation of the Flame Spheroidisation Process for the Rapid Manufacture of Fe_3O_4-Based Porous and Dense Microspheres. *Molecules* **2023**, *28*, 2523. https://doi.org/10.3390/molecules28062523

Academic Editor: Igor Djerdj

Received: 7 February 2023
Revised: 6 March 2023
Accepted: 7 March 2023
Published: 9 March 2023

1. Introduction

From the magnetic materials available, Fe_3O_4-based superparamagnetic nanoparticles (SMNPs) have been most extensively investigated for localised magnetic hyperthermia applications due to their superparamagnetic expression and non-toxicity [1,2], and because iron oxide metabolism is readily achieved by the heme oxygenase-1 gene which generates haemoglobin and promotes cellular iron homeostasis [3]. Related ferrites, such as $NiFe_2O_4$ [4], $MnFe_2O_4$ [5], $CoFe_2O_4$ [6] and $Li_xFe_{3-x}O_4$ [7], have also been investigated to improve magnetic strength and thermal stability. However, the inherent toxicity of Ni, Mn, Co and Li limits their application [3]. An alternative approach is to introduce non-magnetic Ca^{2+} into the ferrite crystalline structure, to generate significant improvements in terms of biocompatibility, whilst maintaining magnetic expression and heating control [8,9]. Non-toxic calcium ferrites have been shown to metabolise safely within the body [10,11], making them appropriate for a range of biomedical applications, including magnetic hyperthermia. Biomedical investigations using calcium ferrites have been reported in relation to drug-delivery systems [8,9,12,13] and cytocompatibility [8,10,12,14]. Approaches combining metal cations and calcium ferrites for therapeutic applications have also been explored [9,11,15–18]. The present challenge is to develop these materials into practical morphologies for enhanced biomedical investigations.

Microspheres have been widely investigated for a variety of healthcare applications. Porous microspheres, in particular, offer functional advantages, including the incorporation

of payloads (drugs, cells, biologics, etc.) on external surfaces and within their pores [19,20], along with cell attachment and proliferation over the enhanced surface area available [19]. However, biomedical applications of microspheres are dependent strongly on the types of material employed. In the case of polymer-based microspheres, applications have included targeted drug delivery, tissue engineering and regenerative medicine [21,22]. Whilst ceramic and glass-based microspheres are more commonly associated with tissue regeneration applications, e.g., bone repair [23,24], orthopaedics [25], dental [26] and cancer therapeutics (radiotherapy) [27], along with magnetic hyperthermia.

Raising the temperature of cancerous regions of the body to 40–45 °C to induce cell death is the basis for hyperthermia treatment [3,28,29], whereas magnetic hyperthermia treatment utilises an alternating magnetic field (AMF) to produce localised heat using magnetic particles [30]. Most research on magnetic hyperthermia has focused on SMNPs, which show remarkable physical and functional properties, useful for magnetic hyperthermia, including remote manipulation mediated by an AMF [31], the ability to cross biological barriers due to their small size (10–100 nm) [32], biocompatibility [33] and capability to transform AMF energy into heat [31]. A limitation of SMNPs' use on local magnetic hyperthermia relates to the insufficient amount of heat generated by a single nanoparticle [34,35], with the agglomeration of large quantities of SMNPs required to produce sufficient heat to trigger cancer cell death [36,37]. However, agglomeration can have a negative effect on superparamagnetic properties and heat performance of SMNPs [36,38]. Alternatively, it has been suggested to use larger ($\geq$1 μm) ferromagnetic particles [39].

Ceramic and glass-ceramic microspheres can be manufactured by a variety of methods, including vertical furnace drop tower [19], sol-gel [40], spray drying [41] and flame spheroidisation approaches [42]. In particular, the single-stage, flame spheroidisation process offers a rapid, cost-effective [19,25] and promising approach for the large-scale manufacture of porous and dense microspheres. The feeding of fine-scale particles into a high-temperature flame causes them to melt and acquire spherical form upon ejection from the flame as a consequence of surface tension and solidification upon cooling [42,43]. A variety of physical and process parameters associated with flame spheroidisation can affect the morphology of the end microsphere products [43], including feedstock particle size, material melting temperature, flame temperature and gas flow ratio.

In this context, we report on the flame spheroidisation-processing of Fe_3O_4:$CaCO_3$ powders, and the optimisation of mass ratio and O_2/C_2H_2 gas flow conditions for the production of porous and dense, calcium ferrite microspheres, with highly controlled microsphere sizes and morphologies. Complementary magnetisation and induction heating investigations have also been undertaken to validate the potential of $Ca_2Fe_2O_5$ microspheres for magnetic hyperthermia applications.

2. Results

2.1. Effect of Fe_3O_4:$CaCO_3$ Mass Ratio

2.1.1. Size Range of Microsphere Reaction Products (Unsieved)

Figure 1a–c shows low magnification SE images of flame-spheroidised products formed from Fe_3O_4:$CaCO_3$ precursor/porogen materials, with mass ratios of Figure 1a—3:1, Figure 1b—1:1 and Figure 1c—1:3, respectively, using a gas flow setting of 2.5:2.5 in all cases.

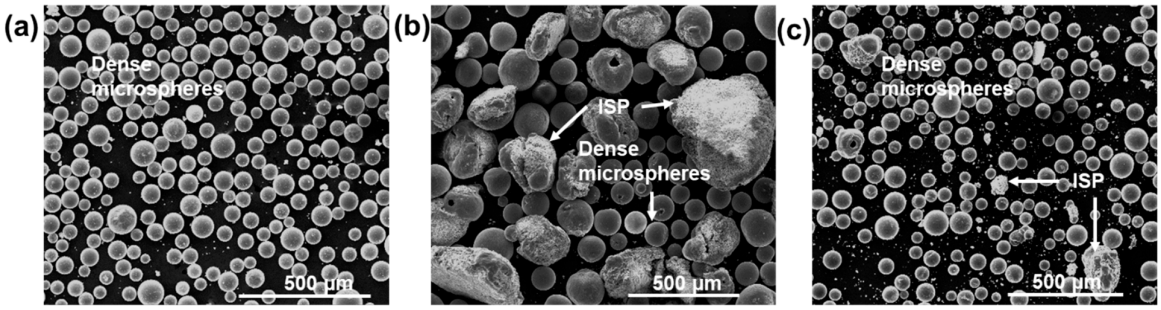

Figure 1. SE images of flame-spheroidised Fe_3O_4:$CaCO_3$, using starting $\leq$ 5 µm sized Fe_3O_4 powders. Mass ratios: (**a**) 3:1, (**b**) 1:1 and (**c**) 1:3, (unsieved), showing dense microspheres and irregular-shaped particles. ISP: irregular-shaped particles.

As summarised in Table 1, a mass ratio of 1:1 led to the production of a mixture of dense microspheres and larger, irregular-shaped particles (Figure 1b). Notably, a 3:1 mass ratio (Fe_3O_4-rich) generated a consistent yield of dense microspheres with very few irregular-shaped particles (Figure 1a), whereas a 1:3 mass ratio ($CaCO_3$-rich) produced a similar mixture of dense microspheres and few irregular-shaped particles (Figure 1c).

Table 1. Size range of flam-spheroidised reaction products (dense microspheres, irregular-shaped particles (ISP), and microspheres with surface porosity), as a function of precursor to porogen mass ratio.

Mass Ratio Fe_3O_4:$CaCO_3$	Gas Flow Setting/arb. Unit	Dense Microspheres/µm	ISP/ µm	Microspheres with Surface Porosity/µm
3:1	2.5:2.5	35–165	75–475	No
1:1		65–210	205–465	
1:3		40–145	40–195	

2.1.2. Structural Characterisation (Unsieved Microspheres)

XRD investigations were performed to appraise the structural integrity of unsieved reaction products as a function of the flame-spheroidisation processing conditions. Figure 2 shows XRD patterns for the flame-spheroidised products (mass ratios 3:1, 1:1 and 1:3) corresponding to the sample sets imaged in Figure 1a–c. Structural analyses confirmed the presence of varying proportions of $Ca_2Fe_2O_5$ (srebrodolskite) (ICDD PDF no. 00-047-1744), Fe_3O_4 (magnetite) (ICDD PDF no. 01-087-0244), Fe_2O_3 (hematite) (ICDD PDF 00-033-0664), $CaCO_3$ (calcium carbonate) (ICDD PDF no. 00-047-1743) and CaO (calcium oxide) (ICDD PDF no. 00-048-1467).

As outlined in Table S1 (see Supplementary Materials), a mass ratio of 1:1 produced strong signatures for Fe_2O_3, $Ca_2Fe_2O_5$ and (unreacted) $CaCO_3$, along with a medium signature for (unreacted) Fe_3O_4. A mass ratio of 3:1 (Fe_3O_4-rich) revealed a dominant Fe_2O_3 signature, with medium Fe_3O_4 and $Ca_2Fe_2O_5$ signatures, and a weak signature for $CaCO_3$. A mass ratio of 1:3 ($CaCO_3$-rich) showed strong signatures for $Ca_2Fe_2O_5$ and CaO, medium signatures for Fe_2O_3 and $CaCO_3$, and a weak signature for Fe_3O_4. In particular, the progression towards higher porogen content (mass ratio from 3:1 to 1:3) was associated with a reduction in magnetite (Fe_3O_4) and hematite (Fe_2O_3) peak intensities and a consolidation of intensities attributable to srebrodolskite ($Ca_2Fe_2O_5$), $CaCO_3$ and CaO (reacted porogen).

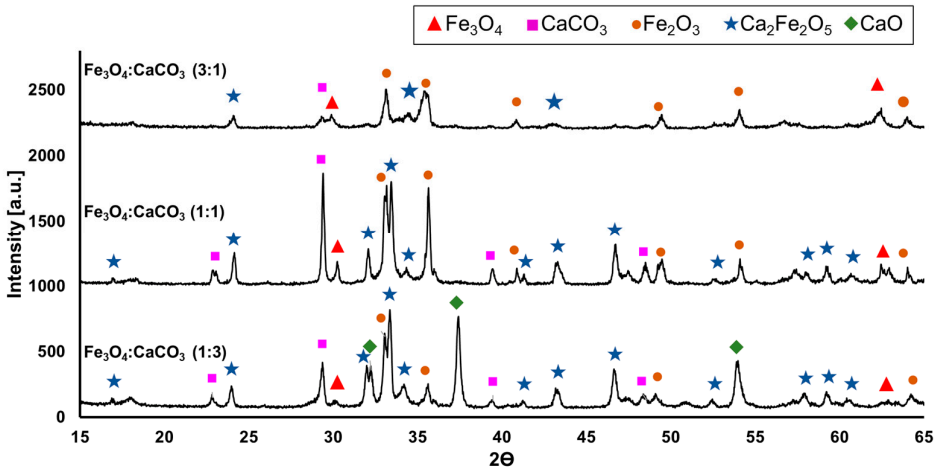

Figure 2. XRD patterns for flame-spheroidised Fe_3O_4:$CaCO_3$ (mass ratios 3:1, 1:1 and 1:3).

2.1.3. Microsphere Magnetic Properties (Sieved)

Magnetisation measurements provided information on the magnetic properties of flame spheroidised microspheres and clarified the effect of Fe_3O_4:$CaCO_3$ mass ratio on magnetic expression. For all samples, the magnetisation curves were indicative of typical ferrimagnetic behaviour. Figure 3 presents magnetisation curves for the sieved flame-spheroidised products (mass ratios 3:1, 1:1 and 1:3; gas flow setting 2.5:2.5). As summarised in Table 2, progression towards increased porogen (mass ratio from 3:1 to 1:3) was accompanied by a decrease in magnetisation, consistent with a lowering of iron content.

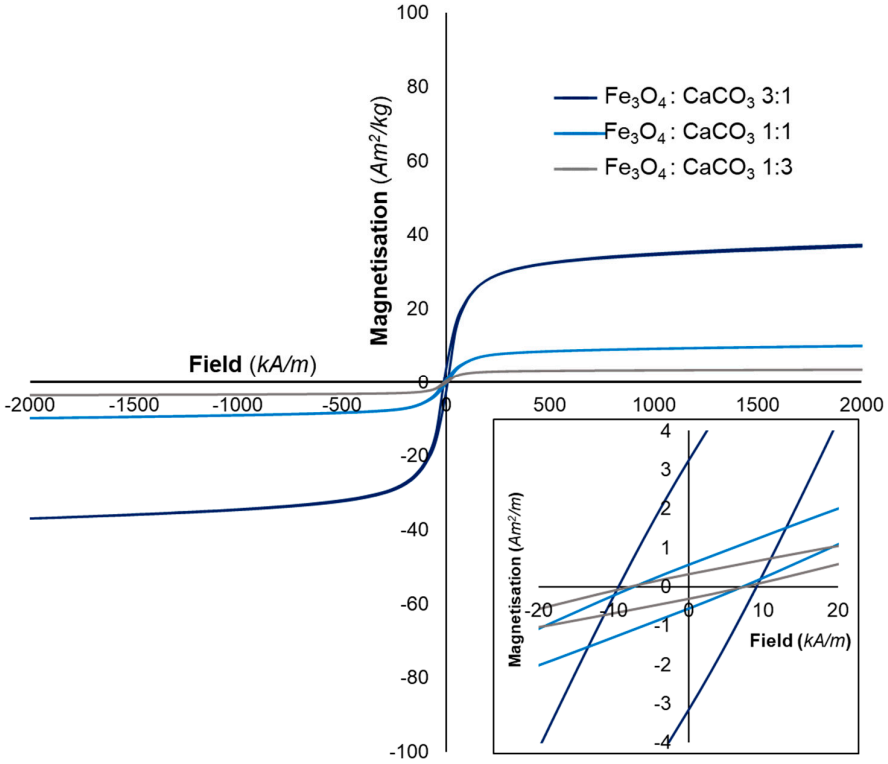

Figure 3. Magnetisation curves for flame-spheroidised Fe_3O_4:$CaCO_3$ (mass ratios 3:1, 1:1 and 1:3; GFS 2.5:2.5) at 26.85 °C. Inset figure provides evidence of remanent magnetisation in all cases.

Table 2. Magnetic measurements of flame-spheroidised products as a function of precursor to porogen mass ratio.

Mass Ratio Fe_3O_4:$CaCO_3$	Gas Flow Setting	Magnetic Saturation/M_s	Remanent Magnetisation/M_r	Coercive Field/ H_c	
	Arb. Units	Am^2/kg (emu/g)	Am^2/kg (emu/g)	(kA/m)	(Oe)
3:1	2.5:2.5	36	3.3	9.1	115
1:1		10.1	0.6	7.0	87.5
1:3		3.6	0.3	7.2	90

2.1.4. Fine Scale Morphologies and Compositional Analyses (Sieved and Sectioned)

Figure 4a–c presents BSE images and MLA mapping analyses, revealing fine-scale morphological details and clarifying the outcomes of compositional dependencies on the precursor-porogen mass ratio of the sieved microsphere products, extracted from the sample sets presented in Figure 1.

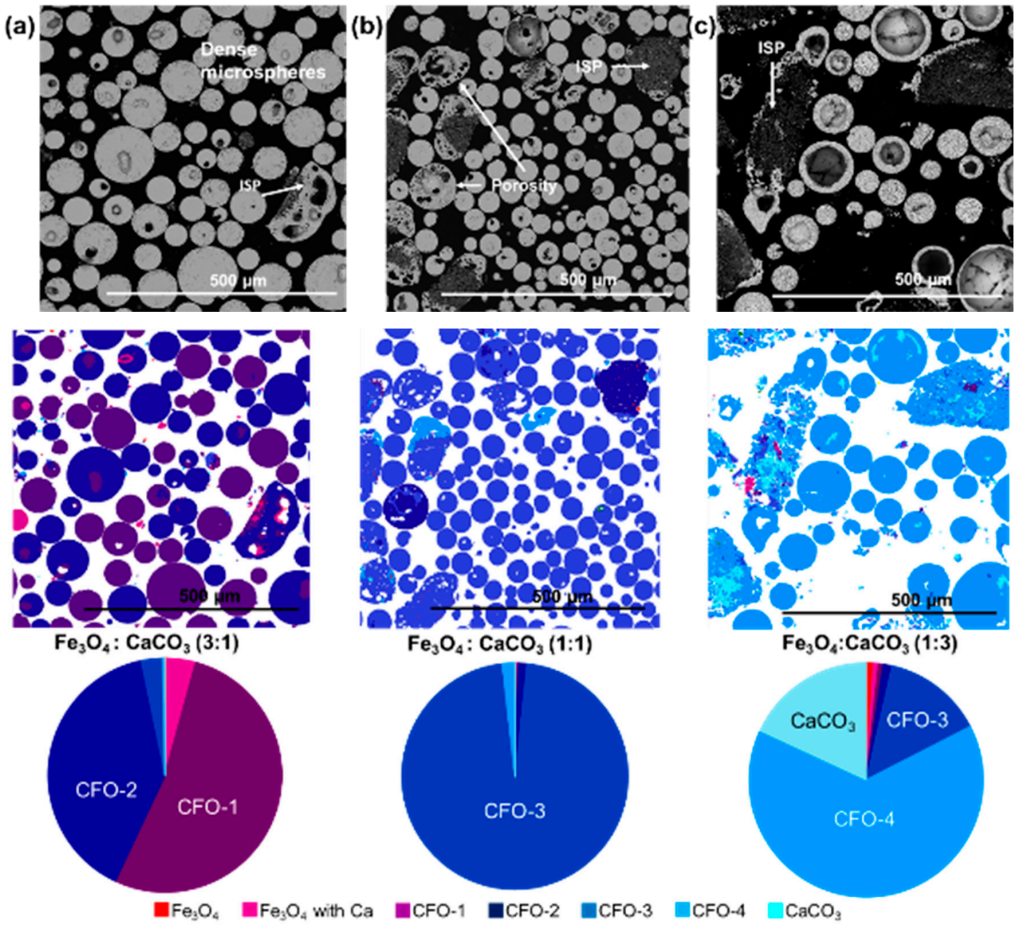

Figure 4. BSE images, MLA compositional analyses and associated pie-charts showing mineral proportions (wt%) of flame spheroidised Fe_3O_4:$CaCO_3$ as a function of mass ratio: (**a**) 3:1, (**b**) 1:1 and (**c**) 1:3; following sieving and sectioning, illustrating microsphere porosity, ISP, and dense microspheres. ISP: irregular-shaped particles; CFO: calcium iron oxide.

Varying levels of internal porosity were observed for all sample sets. For the case of flame-spheroidised Fe_3O_4:$CaCO_3$ with mass ratio 1:1/gas flow setting 2.5:2.5 (Figure 4b), upon sectioning, direct evidence was provided for the development of low and high levels of internal porosity within dense microspheres and larger irregular-shaped particles, respec-

tively. For the case of flame-spheroidised processed precursor-rich powder (mass ratio 3:1; gas flow setting 2.5:2.5; Figure 4a), the evidence showed the development of comparatively lower levels of internal porosity within dense microspheres and few irregular-shaped particles. Conversely, for the case of flame-spheroidised processed porogen-rich powder (mass ratio 1:3; gas flow setting 2.5:2.5; Figure 4c), a variety of dense and irregular-shaped developed morphologies with significantly higher levels of internal porosity was revealed.

In particular, and as highlighted in Table 3, compositional differences were evident across the mass ratio sample set, with a strong trend towards the development of banded calcium iron oxide (CFO) compositions, the most prevalent of which being srebrodolskite ($Ca_2Fe_2O_5$, denoted CFO-3—$Ca_2Fe_2O_5$; Supplementary Materials, Table S2 and Figure S1). As anticipated, a progressive decrease in precursor content or increment in porogen content (mass ratio 3:1 to 1:3) was directly accompanied by a lowering of Fe levels and elevation of Ca levels throughout the microsphere products.

Table 3. Mineral proportion (wt%) of flame spheroidised products, as a function of precursor to porogen mass ratio.

Mass Ratio Fe_3O_4:$CaCO_3$	Gas Flow Setting/arb. Units	Fe_3O_4/wt%	Fe_3O_4 with Ca/wt%	CFO-1/wt%	CFO-2/wt%	CFO-3 $Ca_2Fe_2O_5$/wt%	CFO-4/wt%	$CaCO_3$/wt%	Particles Analysed via MLA
3:1	2.5:2.5	0.3	3.9	52.7	39.7	3.0	0.2	0.1	9544
1:1		0.1	0.3	0.1	1.2	96.5	1.8	0.0	4064
1:3		1.0	0.7	0.7	1.2	13.9	64.4	18.1	23,851

For the case of flame spheroidised Fe_3O_4:$CaCO_3$ with a mass ratio of 1:1 gas flow setting 2.5:2.5 (Figure 4b; Supplementary Materials, Figure S2), MLA mapping provided direct evidence for high levels of homogeneity of CFO-3—$Ca_2Fe_2O_5$. For the case of flame-spheroidised precursor-rich powder (mass ratio 3:1; gas flow setting 2.5:2.5; Figure 4a, Supplementary Materials, Figure S3), the evidence comprised two dominant CFO levels (denoted CFO-1 and CFO-2; Supplementary Materials, Table S2). Both of these samples (Figure 4a,b) showed complete consumption of the precursor and porogen, with no evidence of residual Fe_3O_4 nor $CaCO_3$. Conversely, for the case of flame spheroidised porogen-rich powder with a mass ratio of 1:3 (Figure 4c, Supplementary Materials, Figure S4), the data revealed a mixture of CFO compositions dominated by Ca excess (CFO-4; Supplementary Materials, Table S2), along with larger irregular-shaped particles comprising unreacted porogen.

Complementary, energy-dispersive X-ray spectroscopy (EDS) mappings validated elemental compositions and fine-scale details for the microsphere products, as a function of mass ratios of 3:1, 1:1 and 1:3 (Supplementary Materials, Figure S5 and Table S3).

2.2. Effect of O_2/C_2H_2 Gas Flow Setting

2.2.1. Size Range of Microsphere Reaction Products (Unsieved)

Figure 5a,b shows low magnification SE images of flame-spheroidised Fe_3O_4:$CaCO_3$ products, for precursor to porogen (Fe_3O_4:$CaCO_3$) mass ratio 1:1, with gas flow settings of Figure 5a—2:2 and Figure 5b—3:3, respectively.

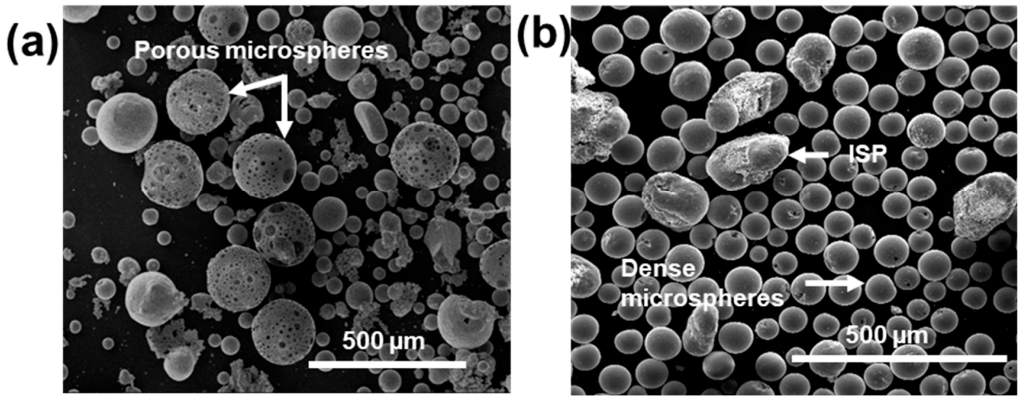

Figure 5. SE images of flame-spheroidised Fe_3O_4:$CaCO_3$ (1:1 mass ratio). Gas flow settings: (**a**) 2:2 and (**b**) 3:3 (unsieved). ISP: irregular-shaped particles.

As summarised in Table 4, a lower gas flow setting of 2:2 (mass ratio 1:1) resulted in a consistent yield of highly porous microspheres, along with a small dense microsphere and very few irregular-shaped particles (Figure 5a). Comparatively, an increased gas flow setting of 3:3 (mass ratio 1:1) resulted in dense microspheres and few irregular-shaped particles (Figure 5b). Notably, only the gas flow setting 2:2 (mass ratio 1:1) processing conditions resulted in the production of microspheres with visible evidence for porosity (pore size range 1.8–64.5 µm; mean pore size 13.1 µm, SD 12.6 µm; ImageJ software).

Table 4. Size range of flame spheroidised reaction products (dense microspheres, irregular-shaped particles (ISP), and microspheres with surface porosity), as a function of gas flow setting.

Mass Ratio Fe_3O_4:$CaCO_3$	Gas Flow Setting /arb. Unit	Dense Microspheres/µm	ISP/ µm	Microspheres with Surface Porosity/µm
1:1	2:2	35–80	15–105	125–180
	2.5:2.5	65–210	205–465	No
	3:3	55–150	175–210	No

2.2.2. Fine Scale Morphologies and Compositional Analyses (Sieved and Sectioned)

Figure 6a,b show BSE images and MLA mineral mapping analyses, extracted from the sample sets presented in Figure 5, presenting fine-scale morphological details of the sieved microsphere products and clarifying the compositional dependencies on gas flow setting. Interestingly, significant levels of internal porosity were revealed for both sample sets. For the case of the higher gas flow setting 3:3, moderate levels of internal porosity were associated with the microspheres and a few irregular-shaped products (Figure 6b). Whereas, for gas flow setting 2:2, a variety of developed porosities was evident, including high levels of interconnected porosity for the case of larger microspheres (125–180 µm) (Figure 6a).

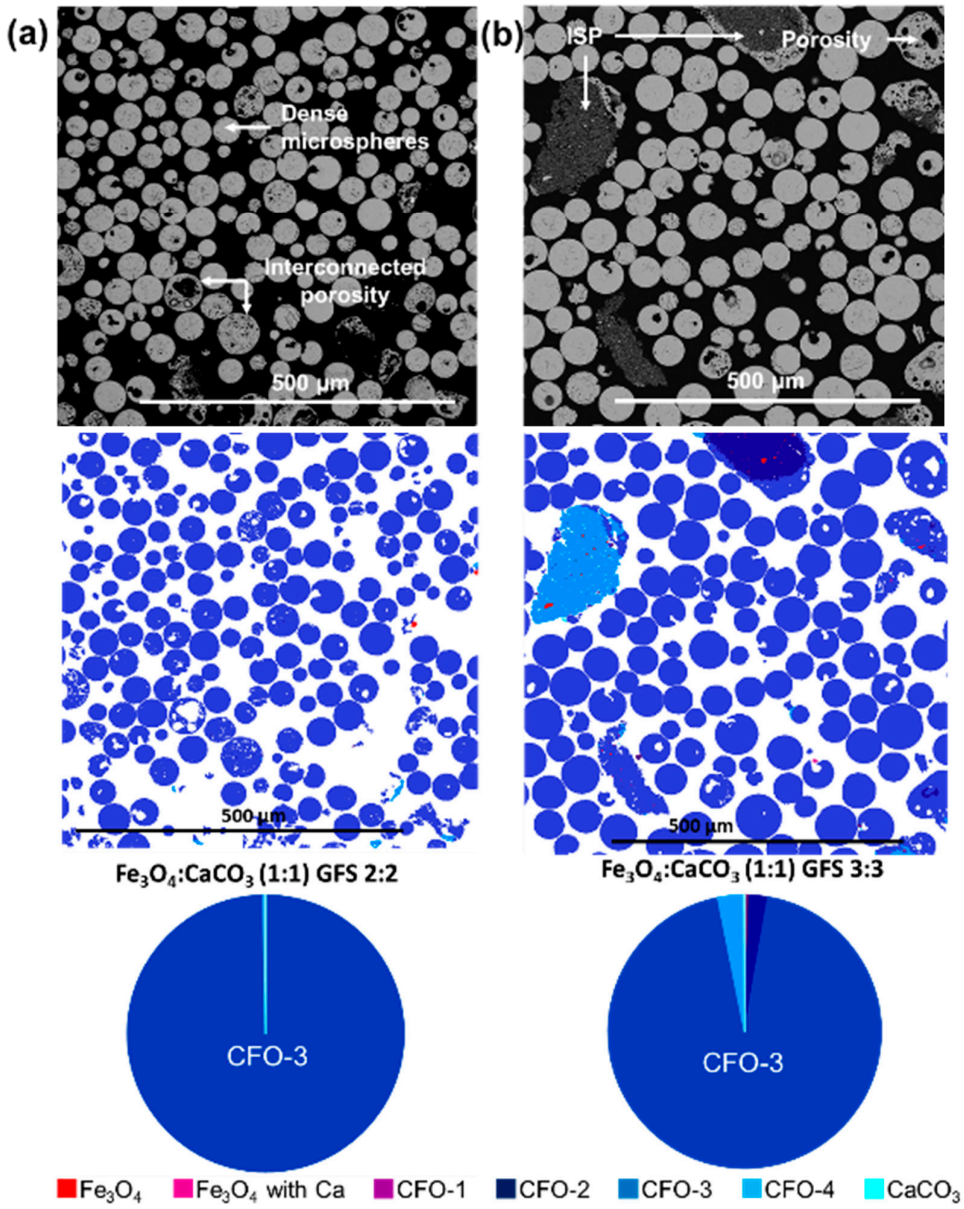

Figure 6. BSE images, MLA compositional analysis and associated pie-charts showing the mineral proportions (wt%) of flame-spheroidised Fe_3O_4:$CaCO_3$ (mass ratio 1:1) microspheres: (**a**) 2:2 and (**b**) 3:3, following sieving and sectioning, illustrating microspheres, porosity and minerals obtained. Mineral references shown on Table S2. GFS: gas flow setting.

As highlighted in Table 5, high levels of sample homogeneity were maintained, as a function of the gas flow setting, with CFO-3 srebrodolskite ($Ca_2Fe_2O_5$) as the dominant phase for all mass ratio 1:1 sample sets. For the case of gas flow setting 3:3, the $Ca_2Fe_2O_5$ proportion decreased slightly compared to gas flow setting 2.5:2.5 (Tables 3 and 5), whilst a small amount of CFO-2 and CFO-4 was evident (Figure 6b; Supplementary Materials, Figure S6). Notably, for the case of gas flow setting 2:2, the highest levels of $Ca_2Fe_2O_5$ homogeneity (99.6 wt%) were returned (Figure 6a; Supplementary Materials, Figure S7).

Table 5. Mineral proportion (wt%) of microsphere products as a function of gas flow setting.

Fe_3O_4:$CaCO_3$ Mass Ratio	Gas Flow Setting	Fe_3O_4/wt%	Fe_3O_4 with Ca/wt%	CFO-1/wt%	CFO-2/wt%	CFO-3/wt%	CFO-4/wt%	$CaCO_3$/wt%	Particles Analysed via MLA
1:1	2:2	0.0	0.0	0.0	0.1	99.6	0.1	0.1	1560
	2.5	0.1	0.3	0.1	1.2	96.5	1.8	0.0	4064
	3:3	0.1	0.1	0.4	2.1	94.1	3.0	0.1	4127

It was noted that the flame spheroidised Fe_3O_4:$CaCO_3$ (1:1 mass ratio; 2:2 gas flow setting) samples revealed the highest levels of compositional uniformity and good levels of interconnected porosity. Further magnetic characterisation and induction heating investigations of these materials were performed.

2.3. $Ca_2Fe_2O_5$ Magnetic Microspheres (Mass Ratio 1:1; Gas Flow Setting 2:2)

2.3.1. Magnetic Properties of $Ca_2Fe_2O_5$ Microspheres

Figure 7 presents magnetisation curves for the precursor/porogen mixture 1:1 Fe_3O_4:$CaCO_3$, prior and post flame spheroidisation, compared to Fe_3O_4 dense microspheres processed in isolation, i.e., without $CaCO_3$ porogen. As summarised in Table 6, the incorporation of porogen into the mixture led to a decrease of magnetisation saturation values. Nevertheless, it was noted that Fe_3O_4:$CaCO_3$ flame-spheroidised products still showed significant magnetic saturation values (8.9 Am^2/kg).

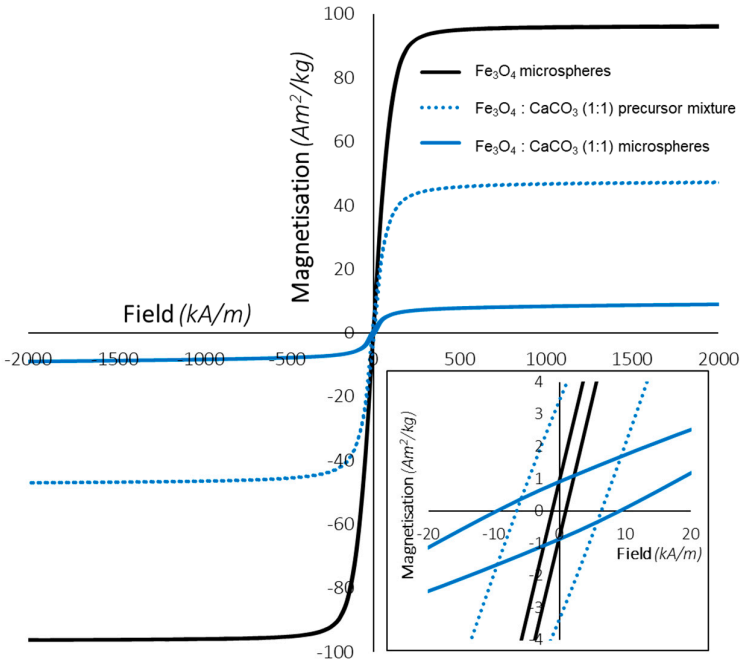

Figure 7. Hysteresis loop measurements for flame-spheroidised Fe_3O_4 microspheres, compared to Fe_3O_4:$CaCO_3$ (mass ratio 1:1) precursor powders and microsphere products, at 26.85 °C. Inset figure provides evidence of remanent magnetisation in all cases.

Table 6. Magnetic saturation, remanent magnetisation and coercive field values of Fe_3O_4 dense microspheres, and Fe_3O_4:$CaCO_3$ (mass ratio 1:1) mixtures before and after flame-spheroidisation.

Sample	Magnetic Saturation	Remanent Magnetization	Coercive Field/Hc	
	Am^2/kg (emu/g)	Am^2/kg (emu/g)	(kA/m)	(Oe)
Fe_3O_4 dense microspheres	96.3	0.8	0.5	6.7
Fe_3O_4:$CaCO_3$ (1:1) starting powders	47.0	3.6	6.7	84.9
Fe_3O_4:$CaCO_3$ (1:1) microspheres	8.9	0.9	8.7	109

2.3.2. Induction Heating Studies

The potential of $Ca_2Fe_2O_5$ microspheres for magnetic-mediated hyperthermia was evaluated via induction heating (Table 7). Figure 8 shows the evolution of temperature for the most homogeneous flame-spheroidised $Ca_2Fe_2O_5$ sample (mass ratio 1:1, gas flow setting 2:2), along with Fe_3O_4 and $CaCO_3$ starting powders by way of control. The Fe_3O_4 powder showed high levels of induction heating, up to ~130 °C, but with an evident lack of heating control, whilst $CaCO_3$ powder showed no induction heating as anticipated. Notably, homogeneous $Ca_2Fe_2O_5$ microspheres exhibited highly controlled heating to a constant level of 43.7 °C which remained stable upon voltage decrease (150 to 35 V).

Table 7. Experimental parameters for induction heating investigations.

Voltage/ V	Power/ W	Current/ A	Magnetic Field/ kA/m (Oe)	Frequency/ kHz
150	120	0.8	0.10 (1.2)	204
35	20	0.6	0.07 (0.9)	204

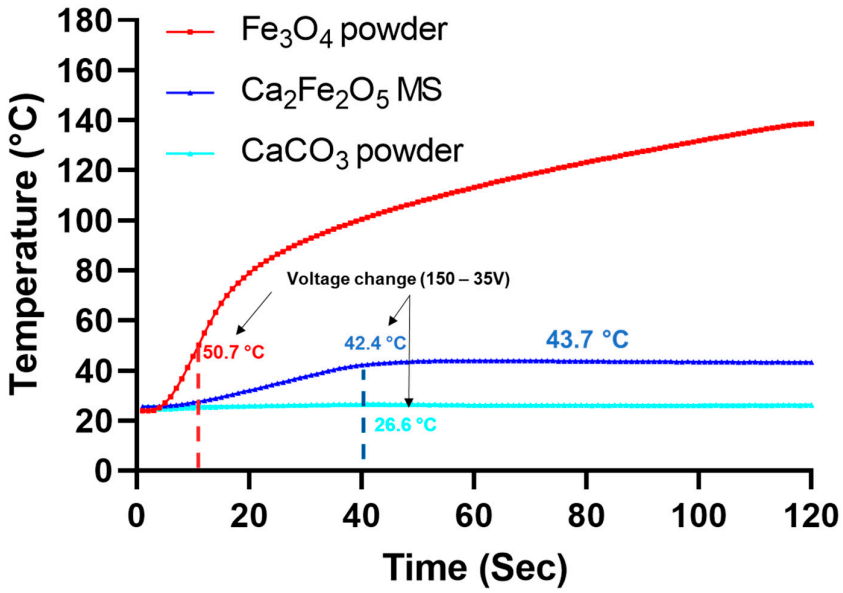

Figure 8. Induction heating curves for flame spheroidised $Ca_2Fe_2O_5$ microspheres (MS), compared with Fe_3O_4 and $CaCO_3$ starting powders. Homogenous $Ca_2Fe_2O_5$ microsphere exhibited highly stabilised temperature control. (All curves display averages of triplicate measurements) (Statistical analysis on Supplementary Materials, Table S4).

3. Discussion

This study reports on the optimisation of the flame-spheroidisation process parameters for the controllable production of magnetite-based porous microspheres (Fe_3O_4 precursor powders/$CaCO_3$ porogen mass ratio, and gas flow setting). Modification of these parameters produced a variety of products in terms of shape (dense and porous microspheres, and irregular-shaped particles), or a mixture of these with distinct magnetic saturation levels and compositions (Fe-Ca excess/deficit). Optimised parameter conditions were identified for the manufacture of compositionally uniform and porous products, with Fe_3O_4:$CaCO_3$ (mass ratio 1:1; gas flow setting 2:2) mixtures producing $Ca_2Fe_2O_5$ microspheres with strong levels of compositional homogeneity and porosity levels (for the case of large porous microspheres). The homogeneous $Ca_2Fe_2O_5$ samples demonstrated controlled delivery of heat (43.7 °C, see Figure 8), highlighting the suitability of these candidate products for magnetic hyperthermia applications.

Figure 9 provides a schematic illustration detailing the development of magnetic microspheres, as a function of mass ratio and gas flow setting parameters. Mass ratio parameters as applied to magnetite/porogen combinations revealed a direct effect on microsphere composition and magnetic properties. Importantly, $Ca_2Fe_2O_5$ (srebrodolskite) was the only calcium iron oxide phase revealed for all Fe_3O_4:$CaCO_3$ flame-spheroidised samples (Figure 2). The suggestion is that rapid cooling and solidification mechanisms associated with the flame-spheroidisation process allowed for the formation of $Ca_2Fe_2O_5$ microsphere structures with modified compositions (excess/deficit of Fe/Ca atoms), i.e., the microsphere products retained structural integrity for all mass ratio cases but presented Fe/Ca variations according to elemental availability. This could also be attributed to the unusual capacity of $Ca_2Fe_2O_5$ to support a number of defects [44,45]. Indeed, this phenomenon was reinforced by compositional analyses of sieved samples. MLA mappings (Figure 4) highlighted a clear trend towards iron deficit/calcium excess, as the mass ratio progressed from 3:1 towards 1:3, with a mass ratio of 1:1 showing the highest levels of homogeneity (CFO-3, denoted as $Ca_2Fe_2O_5$). This compositional trend emphasised the importance of maximum consumption of the starting materials occurring for a mass ratio of 1:1 and gas flow setting of 2.5:2.5; in which case MLA data showed no evidence for any unreacted Fe_3O_4 and $CaCO_3$ from this sample. It should be noted that sieving acted simply to improve sample homogeneity by removing excess, small, unreacted Fe_3O_4 and $CaCO_3$, and Fe_2O_3 reacted powders. In contrast, Fe-rich samples (mass ratio 3:1) showed poor compositional uniformity, with two banded calcium iron oxide minerals observed (CFO-1 and CFO-2). Similarly, Ca-rich samples (mass ratio 1:3) were associated with low porogen consumption, along with irregular-shaped particles containing an excess of unreacted $CaCO_3$ and reacted CaO. In addition, the mass ratio parameter also strongly influenced the microsphere magnetic properties. An increase in porogen content (from Fe_3O_4:$CaCO_3$ 3:1 to 1:3) was directly related to a decrease in magnetic saturation and remanent magnetisation. This was attributed to the incorporation of paramagnetic calcium atoms within the srebrodolskite structure ($Ca_2Fe_2O_5$), as a function of mass ratio. In this context, a report [46] is noted on the incorporation of Gd^{3+} within nanocrystalline iron oxide particles produced by an extraction pyrolytic technique, with hysteresis loops measured via vibrating sample magnetometry (VSM; magnetic field max. 795.7 kA/m) as a function of concentration (mol%) and temperature (at much slower heating rates compared to the rapid flame spheroidisation process). An increase in Gd^{3+} content (from 12.5 to 75 mol%) was related directly to a decrease in magnetic saturation values and remanent magnetisation, similar to the case of $CaCO_3$. Notably, the flame spheroidisation process leads to the formation of metastable products with modified ferromagnetic properties.

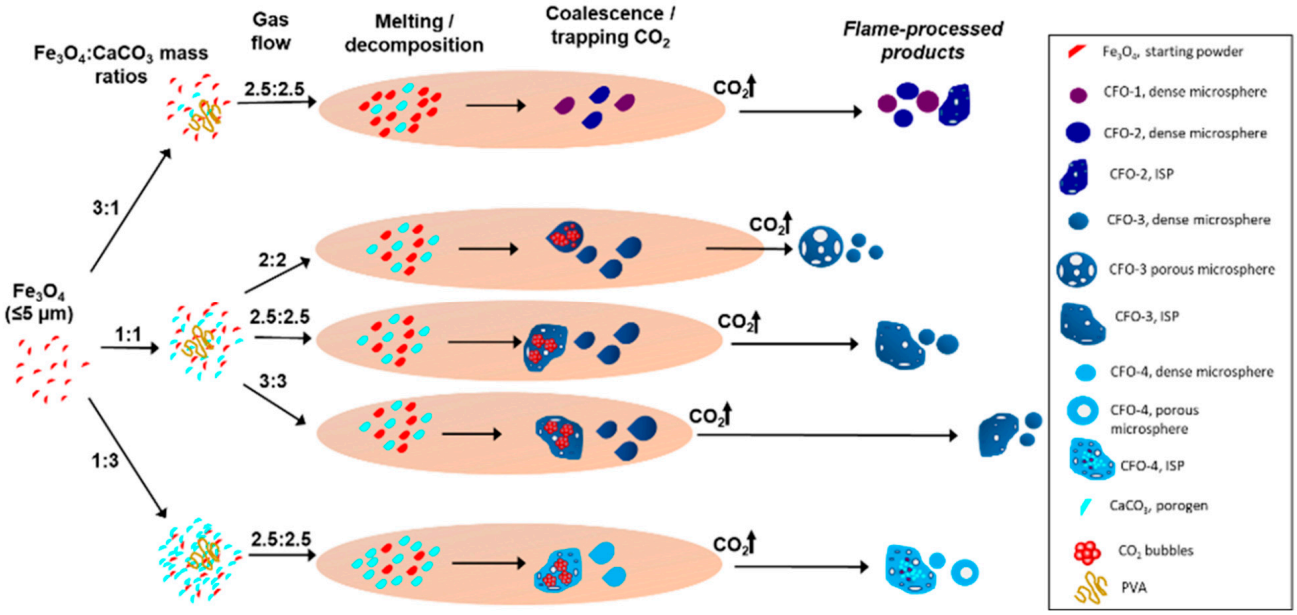

Figure 9. Flame spheroidisation of Fe_3O_4:$CaCO_3$ microsphere products, as a function of mass ratio and gas flow settings.

The parameter of the gas flow setting also influenced the development of porosity within the microspheres. Two types of porosity were identified for this sample set: i.e., internal pores (either interconnected or not) and surface pores. It is considered that surface pores formed via molten droplets trapping and releasing CO_2 gas bubbles produced during porogen decomposition ($CaCO_3 \rightarrow CaO + CO_2$). In contrast, internal pores were created within molten drops as a consequence of unreleased CO_2 gas bubbles, during rapid solidification. Indeed, it is noted that an increment in porogen concentration combined with an elevated gas flow setting, i.e., 3:3, was associated with higher internal porosity levels. Conversely, surface pores (with interconnected porosity) were more strongly associated with increased porogen content, albeit with a 2:2 gas flow setting. This effect was attributed to the increased residence time of molten droplets within the oxy-acetylene flame, as a determining factor for the development of microsphere porosity. Considering that particle temperature is directly related to the residence time of the particle within the flame [47,48], a gas flow setting of 2:2 would facilitate CO_2 trapping and release, and maximise the number of reacted precursor/porogen powders, thereby producing fewer irregular-shaped particles. Furthermore, flame length could be controlled by adjusting the gas flow ratio [49]. As illustrated in Figure 9, the flame length decreased with increasing gas flow settings (from 2:2 to 3:3), consequently influencing particle residence time within the flame and cooling rate. In addition, polyvinyl alcohol (PVA) promoted the binding of Fe_3O_4 precursors with $CaCO_3$ porogen particles, by helping to hold the agglomerated masses together. Accordingly, it is suggested that porous microspheres were produced from the agglomeration of Fe_3O_4:$CaCO_3$ particles, with rapid melting and coalesce leading to the production of melt pools rendered spherical by surface tension, in advance of rapid solidification and phase separation, as appropriate.

Induction heating measurements demonstrated the capability of $Ca_2Fe_2O_5$ microspheres (mass ratio 1:1; gas flow setting 2:2) to deliver heat in a controllable way, addressing one of the main limitations of magnetic hyperthermia which is controlling the temperature increase to between 40–45 °C [50]. It is suggested that the mechanism of heat generation used in our study was hysteresis loss, as revealed by magnetisation curves showing remanence (Figure 7; Inset figure). This hysteresis loss mechanism is associated with multi-domain, ferro- and ferrimagnetic materials [28,34], different from Néel and Brownian relaxation, responsible for heat generation within single-domain, superparamagnetic nanoparticles (SMNPs). Importantly, the induction heating parameters used

for $Ca_2Fe_2O_5$ measurements were similar to that previously reported for ferromagnetic glass-ceramic microspheres (denoted P40-Fe_3O_4 microspheres) [51] with the distinction that induced magnetic fields were higher for P40-Fe_3O_4 products. Regarding the different magnetic saturation levels between $Ca_2Fe_2O_5$ (8.9 Am^2/kg) and P40-Fe_3O_4 (4 Am^2/kg), there was a requirement to adjust the field in order to reach the target temperature (via induction coil heating). Moreover, magnetic hyperthermia effects may be achieved through the application of weak magnetic fields (<7.95 kA/m) [3]; hence, relatively low magnetic fields were used for these $Ca_2Fe_2O_5$ microsphere induction heating studies. Furthermore, the field frequency (204 kHz) used was within the clinically accepted range for magnetic hyperthermia [3,30,50–55]. Additionally, in the present induction coil experiments the target temperature was achieved rapidly (~40 s), indicating that these microsphere products are promising candidates for reduced periods of magnetic hyperthermia exposure, thereby preventing and reducing patient discomfort [3]. These induction heating measurements showed promising results for the $Ca_2Fe_2O_5$ magnetic microspheres developed. However, for formal validation, this part of the investigation requires further study using alternating magnetic fields, similar to those found in clinical settings.

The formation mechanisms associated with $Ca_2Fe_2O_5$ porous and dense microspheres developed via the flame spheroidisation process have been established [42]. For these magnetic microspheres, Fe_3O_4:$CaCO_3$ particles were fed into a high-temperature oxy-acetylene flame (~3100 °C) where rapid melting and coalescence occurred. The molten particles acquired a spherical shape post exiting the flame due to surface tension. The development of compositionally uniform, porous and dense $Ca_2Fe_2O_5$ microspheres, upon rapid cooling and solidification, was consistent with EDS data (Supplementary Materials, Figure S5 and Table S3) and CaO:Fe_2O_3 (2:1 molar ratio) of the Ca-Fe-O phase diagram [56]. Additionally, fine scale diffraction patterns (SAED data, Supplementary Materials, Figure S8) acquired from $Ca_2Fe_2O_5$ microsphere fragments, confirmed their polycrystalline structure.

Accordingly, to produce porous microspheres with interconnected porosity and high values of compositional homogeneity, the results suggest that optimised flame spheroidisation process conditions should be at the gas flow setting of 2:2, using a magnetite-to-porogen mass ratio of 1:1. It was noted that the formation of compositionally uniform, $Ca_2Fe_2O_5$ porous and dense microsphere products can be achieved by controlling the mass ratio and gas flow setting parameters from the flame spheroidisation process. Moreover, these $Ca_2Fe_2O_5$ microspheres show potential for magnetic hyperthermia applications due to their ability to deliver heat in a controllable way. Additionally, the elevated temperatures of magnetic hyperthermia may improve synergistically the release of certain chemotherapeutic agents, such as cisplatin, cyclophosphamide and bleomycin [57–59]. Hence, the compositionally uniform $Ca_2Fe_2O_5$ microspheres could be explored for drug delivery applications in combination with magnetic hyperthermia.

4. Materials and Methods

4.1. Materials

The starting feedstock comprised mixtures of as-supplied iron(II,III) oxide powder (Fe_3O_4; ≤5 μm, 95%; Merck, Gillingham, UK) and calcium carbonate as porogen ($CaCO_3$, ≤5 μm, 98%; Fisher Scientific UK Ltd, Loughborough, UK.). The magnetite (Fe_3O_4) powder was mixed with $CaCO_3$ using a pestle and mortar and combined with droplets of 2% aqueous solution polyvinyl alcohol (PVA; Merck, UK) to act as a binder, followed by drying at 37 °C for 24 h.

4.2. Flame Spheroidisation Parameters

Fe_3O_4-based microspheres were produced by flame spheroidisation, whereby prepared powders were flame processed using a thermal spray gun (MK74, Metallisation Ltd., Dudley, UK) (Figure 10) [42].

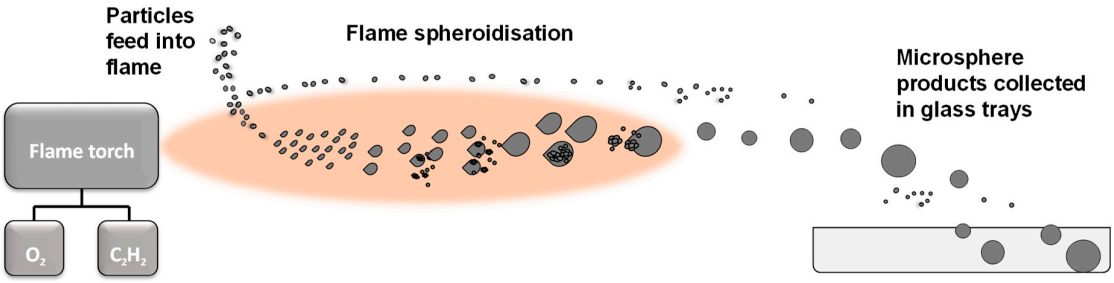

Figure 10. Schematic representation of the single-stage, flame spheroidisation process.

The processed materials were collected using glass trays, placed a short distance away from the thermal spray gun, and stored in glass vials for characterisation. Parameters to evaluate the effects of Fe_3O_4 precursor to $CaCO_3$ porogen mass ratios (3:1, 1:1 or 1:3) and oxy-acetylene gas flow settings (O_2/C_2H_2; 2:2, 2.5:2.5 or 3:3) on the resultant products are summarised in Tables 8 and 9, respectively.

Table 8. Parameters to evaluate the effects of Fe_3O_4:$CaCO_3$ mass ratio.

Fe_3O_4 Size/μm	$CaCO_3$ Size/μm	Mass Ratio Fe_3O_4:$CaCO_3$	Preparation	Oxygen-Acetylene Gas Flow Setting/arb. Unit
≤5	≤5	3:1	Mixed with PVA	2.5:2.5
		1:1		
		1:3		

Table 9. Parameters to evaluate the effects of gas flow setting.

Fe_3O_4 Size/μm	$CaCO_3$ Size/μm	Mass Ratio Fe_3O_4:$CaCO_3$	Preparation	Oxygen-Acetylene Gas Flow Setting/arb. Unit
≤5	≤5	1:1	Mixed with PVA	2:2
				2.5:2.5
				3:3

4.3. Microsphere Characterisation

4.3.1. Microsphere Morphology and Size

Imaging of the as-acquired flame spheroidised products (unsieved) was performed by scanning electron microscopy (SEM; FEI XL30; 5 kV; spot size 2.5; 13.3 mm working distance, secondary electron (SE) imaging mode). Microsphere size distributions were established using ImageJ 1.51h software (National Institutes of Health, Bethesda, MD, USA).

4.3.2. X-ray Diffractometry

Structural characterisation was performed by X-ray diffractometry (XRD; Bruker D8 Advance, Da Vinci design with LYNXEYE XE-T detector in 1D mode; Cu Ka radiation (λ = 0.15406 nm); 40 kV and 40 mA; step size 0.02°; total time/step 29.8 s per datapoint; 21 °C).

4.3.3. Magnetic Characterisation

The microsphere products were then sieved (using a stainless-steel frame; 203 × 50 mm; ≥32 μm mesh; VWR International) to filter out surplus starting material. Complementary magnetisation measurements were performed using a superconducting quantum interference device magnetometer (SQUID; Quantum Design MPMS-3 system; VSM mode; vibration amplitude 1.5 mm; 26.9 °C).

4.3.4. Compositional Characterisation

The sieved microspheres were embedded in a cold epoxy resin and sectioned by sequential mechanical grinding (using 400, 800 and 1200 SiC grit papers) and polishing (6 and 1 μm diamond paste). The polished samples were then cleaned using deionised water and industrial methylated spirit (IMS) and dried before carbon coating. Backscattered electron (BSE) imaging and chemical analyses of sieved and sectioned microspheres were performed via SEM-based mineral liberation analysis (MLA), using an FEI Quanta600 MLA (20 kV; spot size 7) equipped with energy dispersive X-ray spectroscopy (EDS) for compositional analysis and associated Bruker/JKTech/FEI data acquisition software for automated mineralogy.

4.3.5. High Frequency Induction Heating

Induction heating studies of sieved microspheres were performed via high frequency induction (Cheltenham Induction Heating Ltd.; 35–150 V; 20–120 W; 0.6–0.8 A; 204 kHz). Glass vials containing the magnetic microspheres were placed at the centre of a water-cooled copper coil generating an alternating magnetic field, whilst the temperature was measured using a fibre optic temperature sensor (Neoptix Reflex Signal Conditioner). Control samples of starting Fe_3O_4 and $CaCO_3$ powders were also investigated. All measurements were repeated three times.

5. Conclusions

Compositionally uniform, ferromagnetic $Ca_2Fe_2O_5$ porous and dense microspheres have been developed via the rapid, single-stage, flame spheroidisation process using feedstock powder Fe_3O_4:$CaCO_3$ combinations. Morphological, structural and compositional investigations provided evidence of the effect of Fe_3O_4:$CaCO_3$ mass ratio, and O_2/C_2H_2 gas flow setting parameters. Complementary SQUID magnetometry confirmed the ferromagnetic properties of flame-spheroidised products. The potential use of $Ca_2Fe_2O_5$ microspheres (1:1 mass ratio/2:2 gas flow setting) for magnetic hyperthermia applications with a simple, but significant, induction heating measurement (43.7 °C) was shown. The combination of compositional control, high levels of porosity and functional properties (i.e., magnetic and thermal) achieved opens up new opportunities, to explore the application of magnetic microspheres for a range of biomedical challenges.

Supplementary Materials: The following supporting information can be downloaded at: https://www.mdpi.com/article/10.3390/molecules28062523/s1, Table S1: Generalised summary of unsieved flame spheroidised product proportions, as a function of precursor to porogen mass ratio. FS: flame spheroidised; Table S2. Molar constituents (weight percentage) and mineral composition reference; Figure S1. MLA mineral colour code as a function of excess (or deficit) Fe or Ca concentration; Figure S2. Full MLA compositional analysis and modal minerology of flame spheroidised Fe_3O_4:$CaCO_3$ (mass ratio 1:1; gas flow setting 2.5:2.5), following sieving and sectioning, demonstrating high levels of CFO-3-$Ca_2Fe_2O_5$; Figure S3. Full MLA compositional analysis and modal minerology of flame spheroidised Fe_3O_4:$CaCO_3$ (mass ratio 3:1; gas flow setting 2.5:2.5), following sieving and sectioning, demonstrating high levels of CFO-1 and CFO-2; Figure S4. Full MLA compositional analysis and modal minerology of flame spheroidised Fe_3O_4:$CaCO_3$ (MR 1:3; GFS 2.5:2.5), following sieving and sectioning, demonstrating high levels of CFO-4; Figure S5. BSE images and elemental mappings showing iron, calcium and oxygen for flame spheroidised Fe_3O_4:$CaCO_3$ (mass ratios 3:1, 1:1, 1:3), following sieving and sectioning; Table S3. EDS molar concentrations (wt%) and proposed equilibrium phases for flame spheroidised Fe_3O_4:$CaCO_3$ as a function of mass ratio; Figure S6.

Full MLA compositional analysis and modal minerology of flame spheroidisation Fe_3O_4:$CaCO_3$ (mass ratio 1:1; gas flow setting 3:3), following sieving and sectioning, demonstrating high levels of CFO-3-$Ca_2Fe_2O_5$; Figure S7. Full MLA compositional analysis and modal minerology of flame spheroidised Fe_3O_4:$CaCO_3$ (mass ratio 1:1; gas flow setting 2:2), following sieving and sectioning, demonstrating high levels of CFO-3-$Ca_2Fe_2O_5$; Table S4. Statistical analysis on induction heating experiments; Figure S8. Cumulative selected area electron diffraction (SAED) pattern for 120 stacked tilted fields of view, corresponding to compositionally uniform, flame spheroidised Fe_3O_4:$CaCO_3$ (mass ratio1:1; gas flow setting 2:2), i.e. $Ca_2Fe_2O_5$ microsphere fragments following grinding; Table comprising crystal planes and 2-Theta.

Author Contributions: J.M.-D.: Conceptualisation; Methodology; Investigation; Writing—Original draft; Visualisation; Funding acquisition. J.L.W.: Investigation—Induction heating. E.S.: Investigation—MLA. N.A.M.: Investigation—SQUID. P.D.B.: Supervision; Writing—Review & Editing; Visualisation; Funding acquisition. I.A.: Supervision; Writing—Review & Editing; Visualisation; Funding acquisition. All authors have read and agreed to the published version of the manuscript.

Funding: National Council of Science and Technology (Consejo Nacional de Ciencia y Tecnología) (CONACyT) and the Faculty of Engineering, University of Nottingham funded this work. The SQUID characterisation work-package, performed at the Royce Discovery Centre, University of Sheffield was funded by the Henry Royce Institute.

Institutional Review Board Statement: Not applicable.

Informed Consent Statement: Not applicable.

Data Availability Statement: The raw data that support the findings of this investigation is available from the corresponding author upon reasonable request.

Acknowledgments: Jesús Molinar Díaz would like to thank the National Council of Science and Technology (CONACyT) and the Faculty of Engineering, University of Nottingham, for funding this work. With thanks also to the Henry Royce Institute for funding the SQUID characterisation work-package, performed at the Royce Discovery Centre, University of Sheffield. The authors would also like to acknowledge the characterisation facilities made available at the Nanoscale and Microscale Research Centre (nmRC), University of Nottingham, for the use of instruments and facilities; and Michael Fay from the nmRC, for complementary SAED data acquisition.

Conflicts of Interest: The authors declare no conflict of interest.

References

1. McNamara, K.; Tofail, S.A.M. Nanoparticles in biomedical applications. *Adv. Phys. X* **2017**, *2*, 54–88. [CrossRef]
2. Ong, B.H.; Devaraj, N.K.; Matsumoto, M.; Abdullah, M.H. Thermal stability of magnetite (Fe_3O_4) nanoparticles. *MRS Proc.* **2011**, *1118*, K03–K09. [CrossRef]
3. Kumar, C.S.S.R.; Mohammad, F. Magnetic nanomaterials for hyperthermia-based therapy and controlled drug delivery. *Adv. Drug Deliv. Rev.* **2011**, *63*, 789–808. [CrossRef] [PubMed]
4. Bae, S.; Lee, S.W.; Takemura, Y. Applications of $NiFe_2O_4$ nanoparticles for a hyperthermia agent in biomedicine. *Appl. Phys. Lett.* **2006**, *89*, 252503. [CrossRef]
5. Kalaiselvan, C.R.; Thorat, N.D.; Sahu, N.K. Carboxylated PEG-Functionalized $MnFe_2O_4$ Nanocubes Synthesized in a Mixed Solvent: Morphology, Magnetic Properties, and Biomedical Applications. *ACS Omega* **2021**, *6*, 5266–5275. [CrossRef] [PubMed]
6. Karthickraja, D.; Karthi, S.; Kumar, G.A.; Sardar, D.K.; Dannangoda, G.C.; Martirosyan, K.S.; Girija, E.K. Fabrication of core–shell CoFe2O4@HAp nanoparticles: A novel magnetic platform for biomedical applications. *New J. Chem.* **2019**, *43*, 13584–13593. [CrossRef]
7. Srivastava, M.; Alla, S.K.; Meena, S.S.; Gupta, N.; Mandal, R.K.; Prasad, N.K. Magnetic field regulated, controlled hyperthermia with $Li_xFe_{3-x}O_4$ ($0.06 \leq x \leq 0.3$) nanoparticles. *Ceram. Int.* **2019**, *45*, 12028–12034. [CrossRef]
8. Pereira, D.S.M.; Cardoso, B.D.; Rodrigues, A.R.O.; Amorim, C.O.; Amaral, V.S.; Almeida, B.G.; Queiroz, M.-J.R.P.; Martinho, O.; Baltazar, F.; Calhelha, R.C.; et al. Magnetoliposomes Containing Calcium Ferrite Nanoparticles for Applications in Breast Cancer Therapy. *Pharmaceutics* **2019**, *11*, 477. [CrossRef]
9. Cardoso, B.D.; Rodrigues, A.R.O.; Almeida, B.G.; Amorim, C.O.; Amaral, V.S.; Castanheira, E.M.S.; Coutinho, P.J.G. Stealth Magnetoliposomes Based on Calcium-Substituted Magnesium Ferrite Nanoparticles for Curcumin Transport and Release. *Int. J. Mol. Sci.* **2020**, *21*, 3641. [CrossRef]
10. Khanna, L.; Verma, N.K. Synthesis, characterization and in vitro cytotoxicity study of calcium ferrite nanoparticles. *Mater. Sci. Semicond. Process.* **2013**, *16*, 1842–1848. [CrossRef]

11. Kheradmand, A.; Vahidi, O.; Masoudpanah, S.M. Magnetic, hyperthermic and structural properties of zn substituted $CaFe_2O_4$ powders. *Appl. Phys. A* **2018**, *124*, 255. [CrossRef]
12. Bilas, R.; Sriram, K.; Maheswari, P.U.; Sheriffa Begum, K.M.M. Highly biocompatible chitosan with super paramagnetic calcium ferrite ($CaFe_2O_4$) nanoparticle for the release of ampicillin. *Int. J. Biol. Macromol.* **2017**, *97*, 513–525. [CrossRef] [PubMed]
13. Naderi, E.; Aghajanzadeh, M.; Zamani, M.; Sharafi, A.; Naseri, M.; Danafar, H. The Effect of Calcination Temperature on the Anticancer Activity of $CaFe_2O_4$@PVA Nanocarriers: Photodynamic Therapy and Drug Delivery Study. *J. Inorg. Organomet. Polym. Mater.* **2020**, *30*, 5261–5269. [CrossRef]
14. Khanna, L.; Verma, N.K. Biocompatibility and superparamagnetism in novel silica/$CaFe_2O_4$ nanocomposite. *Mater. Lett.* **2014**, *128*, 376–379. [CrossRef]
15. Reyes-Rodríguez, P.Y.; Cortés-Hernández, D.A.; Ávila-Orta, C.A.; Sánchez, J.; Andrade-Guel, M.; Herrera-Guerrero, A.; Cabello-Alvarado, C.; Ramos-Martínez, V.H. Synthesis of Pluronic F127-coated magnesium/calcium ($Mg_{1-x}Ca_xFe_2O_4$) magnetic nanoparticles for biomedical applications. *J. Magn. Magn. Mater.* **2021**, *521*, 167518. [CrossRef]
16. Ruthradevi, T.; Akbar, J.; Suresh Kumar, G.; Thamizhavel, A.; Kumar, G.A.; Vatsa, R.K.; Dannangoda, G.C.; Martirosyan, K.S.; Girija, E.K. Investigations on nickel ferrite embedded calcium phosphate nanoparticles for biomedical applications. *J. Alloys Compd.* **2017**, *695*, 3211–3219. [CrossRef]
17. Jasso-Terán, R.A.; Cortés-Hernández, D.A.; Sánchez-Fuentes, H.J.; Reyes-Rodríguez, P.Y.; de-León-Prado, L.E.; Escobedo-Bocardo, J.C.; Almanza-Robles, J.M. Synthesis, characterization and hemolysis studies of $Zn_{(1-x)}Ca_xFe_2O_4$ ferrites synthesized by sol-gel for hyperthermia treatment applications. *J. Magn. Magn. Mater.* **2017**, *427*, 241–244. [CrossRef]
18. Saldívar-Ramírez, M.M.; Sánchez-Torres, C.G.; Cortés-Hernández, D.A.; Escobedo-Bocardo, J.C.; Almanza-Robles, J.M.; Larson, A.; Reséndiz-Hernández, P.J.; Acuña-Gutiérrez, I.O. Study on the efficiency of nanosized magnetite and mixed ferrites in magnetic hyperthermia. *J. Mater. Sci Mater. Med.* **2014**, *25*, 2229–2236. [CrossRef]
19. Hossain, K.M.Z.; Patel, U.; Ahmed, I. Development of microspheres for biomedical applications: A review. *Prog. Biomater.* **2015**, *4*, 1–19. [CrossRef]
20. Cai, Y.; Chen, Y.; Hong, X.; Liu, Z.; Yuan, W. Porous microsphere and its applications. *Int. J. Nanomed.* **2013**, *8*, 1111–1120.
21. Freiberg, S.; Zhu, X.X. Polymer microspheres for controlled drug release. *Int. J. Pharm.* **2004**, *282*, 1–18. [CrossRef] [PubMed]
22. Sousa, A.L.; Ahmed, I. Manufacturing processes for polymeric micro and nanoparticles and their biomedical applications. *AIMS Bioeng.* **2017**, *4*, 46–72.
23. Matamoros-Veloza, A.; Hossain, K.M.Z.; Scammell, B.E.; Ahmed, I.; Hall, R.; Kapur, N. Formulating injectable pastes of porous calcium phosphate glass microspheres for bone regeneration applications. *J. Mech. Behav. Biomed. Mater.* **2020**, *102*, 103489. [CrossRef] [PubMed]
24. Gupta, D.; Hossain, K.M.Z.; Roe, M.; Smith, E.F.; Ahmed, I.; Sottile, V.; Grant, D.M. Long-Term Culture of Stem Cells on Phosphate-Based Glass Microspheres: Synergistic Role of Chemical Formulation and 3D Architecture. *ACS Appl. Bio Mater.* **2021**, *4*, 5987–6004. [CrossRef]
25. Hossain, K.M.Z.; Patel, U.; Kennedy, A.R.; Macri-Pellizzeri, L.; Sottile, V.; Grant, D.M.; Scammell, B.E.; Ahmed, I. Porous calcium phosphate glass microspheres for orthobiologic applications. *Acta Biomater.* **2018**, *72*, 396–406. [CrossRef]
26. Abou Neel, E.A.; Kiani, A.; Valappil, S.P.; Mordan, N.M.; Baek, S.-Y.; Zakir Hossain, K.M.; Felfel, R.M.; Ahmed, I.; Divakarl, K.; Chrzanowski, W.; et al. Glass microparticle- versus microsphere-filled experimental dental adhesives. *J. Appl. Polym. Sci.* **2019**, *136*, 47832. [CrossRef]
27. Milborne, B.; Arafat, A.; Layfield, R.; Thompson, A.; Ahmed, I. The Use of Biomaterials in Internal Radiation Therapy. *Recent Prog. Mater.* **2020**, *2*, 1–34. [CrossRef]
28. Chang, D.; Lim, M.; Goos, J.; Qiao, R.; Ng, Y.Y.; Mansfeld, F.M.; Jackson, M.; Davis, T.P.; Kavallaris, M. Biologically Targeted Magnetic Hyperthermia: Potential and Limitations. *Front. Pharmacol.* **2018**, *9*, 831. [CrossRef]
29. Van der Zee, J. Heating the patient: A promising approach? *Ann. Oncol.* **2002**, *13*, 1173–1184. [CrossRef]
30. Liu, X.; Zhang, Y.; Wang, Y.; Zhu, W.; Li, G.; Ma, X.; Zhang, Y.; Chen, S.; Tiwari, S.; Shi, K.; et al. Comprehensive understanding of magnetic hyperthermia for improving antitumor therapeutic efficacy. *Theranostics* **2020**, *10*, 3793–3815. [CrossRef]
31. Grillone, A.; Ciofani, G. Magnetic Nanotransducers in Biomedicine. *Chemistry* **2017**, *23*, 16109–16114. [CrossRef] [PubMed]
32. Kohane, D.S. Microparticles and nanoparticles for drug delivery. *Biotechnol. Bioeng.* **2007**, *96*, 203–209. [CrossRef] [PubMed]
33. Arami, H.; Khandhar, A.; Liggitt, D.; Krishnan, K.M. In vivo delivery, pharmacokinetics, biodistribution and toxicity of iron oxide nanoparticles. *Chem. Soc. Rev.* **2015**, *44*, 8576–8607. [CrossRef] [PubMed]
34. Velasco, M.V.; Souza, M.T.; Crovace, M.C.; Aparecido de Oliveira, A.J.; Zanotto, E.D. Bioactive magnetic glass-ceramics for cancer treatment. *Biomed. Glasses* **2019**, *5*, 148. [CrossRef]
35. Rabin, Y. Is intracellular hyperthermia superior to extracellular hyperthermia in the thermal sense? *Int. J. Hyperth.* **2002**, *18*, 194–202. [CrossRef] [PubMed]
36. Serantes, D.; Baldomir, D. Nanoparticle Size Threshold for Magnetic Agglomeration and Associated Hyperthermia Performance. *Nanomaterials* **2021**, *11*, 2786. [CrossRef]
37. Engelmann, U.M.; Buhl, E.M.; Draack, S.; Viereck, T.; Ludwig, F.; Schmitz-Rode, T.; Slabu, I. Magnetic Relaxation of Agglomerated and Immobilized Iron Oxide Nanoparticles for Hyperthermia and Imaging Applications. *IEEE Magn. Lett.* **2018**, *9*, 1–5. [CrossRef]

38. Mejías, R.; Hernández Flores, P.; Talelli, M.; Tajada-Herráiz, J.L.; Brollo, M.E.F.; Portilla, Y.; Morales, M.P.; Barber, D.F. Cell-Promoted Nanoparticle Aggregation Decreases Nanoparticle-Induced Hyperthermia under an Alternating Magnetic Field Independently of Nanoparticle Coating, Core Size, and Subcellular Localization. *ACS Appl. Mater. Interfaces* **2019**, *11*, 340–355. [CrossRef]
39. Luderer, A.A.; Borrelli, N.F.; Panzarino, J.N.; Mansfield, G.R.; Hess, D.M.; Brown, J.L.; Barnett, E.H.; Hahn, E.W. Glass-ceramic-mediated, magnetic-field-induced localized hyperthermia: Response of a murine mammary carcinoma. *Radiat. Res.* **1983**, *94*, 190–198. [CrossRef]
40. Łada, W.; Iller, E.; Wawszczak, D.; Konior, M.; Dziel, T. 90Y microspheres prepared by sol-gel method, promising medical material for radioembolization of liver malignancies. *Mater. Sci. Eng. C* **2016**, *67*, 629–635. [CrossRef]
41. Berkmann, J.C.; Herrera Martin, A.X.; Pontremoli, C.; Zheng, K.; Bucher, C.H.; Ellinghaus, A.; Boccaccini, A.R.; Fiorilli, S.; Vitale Brovarone, C.; Duda, G.N.; et al. In Vivo Validation of Spray-Dried Mesoporous Bioactive Glass Microspheres Acting as Prolonged Local Release Systems for BMP-2 to Support Bone Regeneration. *Pharmaceutics* **2020**, *12*, 823. [CrossRef] [PubMed]
42. Molinar Díaz, J.; Samad, S.A.; Steer, E.; Neate, N.; Constantin, H.; Islam, M.T.; Brown, P.D.; Ahmed, I. Flame spheroidisation of dense and porous $Ca_2Fe_2O_5$ microspheres. *Mater. Adv.* **2020**, *1*, 3539–3544. [CrossRef]
43. Gupta, D.; Hossain, K.M.Z.; Ahmed, I.; Sottile, V.; Grant, D.M. Flame-Spheroidized Phosphate-Based Glass Particles with Improved Characteristics for Applications in Mesenchymal Stem Cell Culture Therapy and Tissue Engineering. *ACS Appl. Mater. Interfaces* **2018**, *10*, 25972–25982. [CrossRef] [PubMed]
44. Amorim, B.F.; Morales, M.A.; Bohn, F.; Carriço, A.S.; de Medeiros, S.N.; Dantas, A.L. Synthesis of stoichiometric $Ca_2Fe_2O_5$ nanoparticles by high-energy ball milling and thermal annealing. *Phys. B Condens. Matter* **2016**, *488*, 43–48. [CrossRef]
45. Asenath-Smith, E.; Lokuhewa, I.N.; Misture, S.T.; Edwards, D.D. p-Type thermoelectric properties of the oxygen-deficient perovskite $Ca_2Fe_2O_5$ in the brownmillerite structure. *J. Solid State Chem.* **2010**, *183*, 1670–1677. [CrossRef]
46. Serga, V.; Burve, R.; Maiorov, M.; Krumina, A.; Skaudžius, R.; Zarkow, A.; Kareiva, A.; Popov, A.I. Impact of Gadolinium on the Structure and Magnetic Properties of Nanocrystalline Powders of Iron Oxides Produced by the Extraction-Pyrolytic Method. *Materials* **2020**, *13*, 4147.
47. Hanson, T.C.; Hackett, C.M.; Settles, G.S. Independent control of HVOF particle velocity and temperature. *J. Therm. Spray Technol.* **2002**, *11*, 75–85. [CrossRef]
48. Kamnis, S.; Gu, S. Study of In-Flight and Impact Dynamics of Nonspherical Particles from HVOF Guns. *J. Therm. Spray Technol.* **2010**, *19*, 31–41. [CrossRef]
49. Tikkanen, J.; Gross, K.A.; Berndt, C.C.; Pitkänen, V.; Keskinen, J.; Raghu, S.; Rajala, M.; Karthikeyan, J. Characteristics of the liquid flame spray process. *Surf. Coat. Technol.* **1997**, *90*, 210–216. [CrossRef]
50. Shaterabadi, Z.; Nabiyouni, G.; Soleymani, M. Physics responsible for heating efficiency and self-controlled temperature rise of magnetic nanoparticles in magnetic hyperthermia therapy. *Prog. Biophys. Mol. Biol.* **2018**, *133*, 9–19. [CrossRef]
51. Molinar-Díaz, J.; Woodliffe, J.L.; Milborne, B.; Murrell, L.; Islam, M.T.; Steer, E.; Weston, N.; Morley, N.A.; Brown, P.D.; Ahmed, I. Ferromagnetic Cytocompatible Glass-Ceramic Porous Microspheres for Magnetic Hyperthermia Applications. *Adv. Mater. Interfaces* **2023**, 2202089. [CrossRef]
52. Kouzoudis, D.; Samourgkanidis, G.; Kolokithas-Ntoukas, A.; Zoppellaro, G.; Spiliotopoulos, K. Magnetic Hyperthermia in the 400–1,100 kHz Frequency Range Using MIONs of Condensed Colloidal Nanocrystal Clusters. *Front. Mater.* **2021**, *8*, 638019. [CrossRef]
53. Hergt, R.; Dutz, S. Magnetic Particle Hyperthermia—Biophysical Limitations of a Visionary Tumour Therapy. *J. Magn. Magn. Mater.* **2007**, *311*, 187–192. [CrossRef]
54. Khan, A.S.; Nasir, M.F.; Khan, M.T.; Murtaza, A.; Hamayun, M.A. Study of structural, magnetic and radio frequency heating aptitudes of pure and (Fe-III) doped manganite (La_{1-x} Sr_xMnO_3) and their incorporation with Sodium Poly-Styrene Sulfonate (PSS) for magnetic hyperthermia applications. *Phys. B Condens. Matter* **2021**, *600*, 412627. [CrossRef]
55. Park, J.-H.; Derfus, A.M.; Segal, E.; Vecchio, K.S.; Bhatia, S.N.; Sailor, M.J. Local Heating of Discrete Droplets Using Magnetic Porous Silicon-Based Photonic Crystals. *J. Am. Chem. Soc.* **2006**, *128*, 7938–7946. [CrossRef] [PubMed]
56. Hidayat, T.; Shishin, D.; Decterov, S.; Jak, E. Thermodynamic Optimization of the Ca-Fe-O System. *Metall. Mater. Trans. B* **2015**, *47*, 256–281. [CrossRef]
57. Torres-Lugo, M.; Rinaldi, C. Thermal potentiation of chemotherapy by magnetic nanoparticles. *Nanomedicine* **2013**, *8*, 1689–1707. [CrossRef]
58. Issels, R.D. Hyperthermia adds to chemotherapy. *Eur. J. Cancer* **2008**, *44*, 2546–2554. [CrossRef]
59. Pennacchioli, E.; Fiore, M.; Gronchi, A. Hyperthermia as an adjunctive treatment for soft-tissue sarcoma. *Expert Rev. Anticancer. Ther.* **2009**, *9*, 199–210. [CrossRef]